Numerical analysis of the space charge effect in a MWPC

Ken KATAGIRI, Takuji FURUKAWA, Eri TAKESHITA, and Koji NODA

National Institute of Radiological Sciences, 4-9-1 Anagawa, Inage-ku, Chiba 263-8555, Japan

A numerical calculation code was developed by employing a two-dimensional continuum model for the detailed design of MWPC (Multi-Wire Proportional Chamber) detectors. The temporal evolutions of electron and ion density distributions were evaluated for the time period required by ions to travel between the anode and the cathode. The temporal evolution of the electric field was also calculated to take into account the space charge effect caused by ions. The output signals of an anode, which were multiplied by electron avalanche, were estimated from an electron flux into anodes. By comparing the gain curve evaluated from the output signals with that obtained by theoretical calculations, we confirmed that the numerical code is capable of quantitative estimations of the gas gain. From these results, we discuss the dependence of the output signal on the space charge effect, and the relations between the ion distribution and the space charge effect.

Keywords: Space-charge effect, Avalanche, Gas chamber, MWPC, Gain reduction, Weakly ionized plasmas

1. Introduction

For the beam profile diagnosis of heavy ion cancer therapy in HIMAC (Heavy Ion Medical Accelerator in Chiba) [1], a MWPC (Multi-Wire Proportional Counter) detector have been employed as a beam profile monitor [2]. Due to the high rate incident beams ($\sim 10^8$ pps), a gain reduction of output signals, which is caused by space charge effects, have been observed in the scanning beam experiments at HIMAC [1]. The space charge effect is produced by residual ions around the anodes. The electrons multiplied in avalanches are quickly collected to the anodes. On the other hand, the ions remain in the gas gain region for long period because the drift velocity of the ions is significantly lower than that of electrons. The electric field is distorted by these remaining ions.

In order to improve the gain reduction by optimizing the parameters of MWPCs including an anode radius and the distance between electrodes, we performed a numerical simulations by employing a two-dimensional continuum model. The space charge effect of the gas chamber has been investigated so far by several authors. Assuming the uniform density distribution [3, 4] and the Gaussian density distribution [5] of the space charge, the gain reduction of MWPC was theoretically investigated by means of analytical equations. A numerical calculation employing the continuum model was also performed to analyse the temporal evolution of the electron avalanche in the single-wire proportional counter, under the assumption that the ion motion is negligible for the electron multiplication process [6].

As a first step of the parameter optimization, MWPC was modeled to be a simple geometry including three anode wires and two cathodes. Dependence

author's e-mail: tag410@nirs.go.jp

of the gas gain on applied voltage (gain curve) was evaluated from output signals, which corresponds to the electron flux into the anodes, and compared with that obtained by theoretical calculations. The temporal evolutions of the electron/ion distributions, the electric field distribution, and electric potential distribution were also calculated. To take into account the effects of the ion motion on the space charge effect, the time period to be considered in the calculation was extended significantly longer than the time required by electrons to travel between electrodes. We investigate the influence of the space charge effect on the electron/ion distributions, the potential distribution, and the gas gain.

2. Simulation model

A. Basic equations

Two dimensional analysis was performed to simulate the motion of charged particles in a complicated potential field, which is distorted by the space charge effect. Assuming the establishment of thermal-equilibrium [7], the continuum model was applied to the ionized gas in a He-gas filled chamber. The pressure and the temperature were assumed to be 10^5 Pa and 300 K, respectively. In order to simplify the analysis, particles of electrons (e^-) and positive ions (He^+) were only taken into account. Under the drift-diffusion approximation [7, 8, 9], the ion and electron fluxes are represented as follows:

$$\boldsymbol{\Gamma}_s \equiv n_s \boldsymbol{u}_s = -D_s \nabla n_s \pm n_s \mu_s \boldsymbol{E}. \qquad (1)$$

Here, $\boldsymbol{\Gamma}_s$ is the particle flax, n_s the density, $\boldsymbol{u}_s$ the drift velocity, D_s the diffusion coefficient, μ_s the mobility, and subscript s is the particle species (e: electron, i: ion). Particle conservations for electrons and ions

are expressed by the continuum equation:

$$\frac{\partial n_s}{\partial t} + \nabla \cdot \boldsymbol{\Gamma}_s = G_s - L_s. \tag{2}$$

Here, G_s and L_s are the generation and loss term, respectively. The generation term was derived by using Townsend first ionization coefficient α:

$$G_s = \alpha n_e |\boldsymbol{u}_e|. \tag{3}$$

The radiative recombination, and the three body recombination were included as recombination processes:

$$L_s = \alpha_{RR} n_e n_i + \alpha_{3BR} n_e^2 n_i. \tag{4}$$

Here, α_{RR} and α_{3BR} are the rate coefficient for the radiative recombination and the three body recombination [10], respectively. The swarm parameters (α, μ_s) and the diffusion coefficient D_s were evaluated as a function of the electric field $|\boldsymbol{E}|$ under the local field approximation (LFA). For these parameters, the Poisson equation was concurrently solved:

$$\nabla^2 \phi = -\frac{e(n_i - n_e)}{\varepsilon_0}, \tag{5}$$

$$\boldsymbol{E} = -\nabla\phi. \tag{6}$$

The diffusion coefficient for ions D_i was derived from the Einstein's formula. The diffusion coefficient for electrons D_e was evaluated by using the BOLSIG+ [11], which is the Boltzmann equation solver. The Townsend first ionization coefficient α, and mobility μ_s, were derived from the Siglo Data Base [12].

B. Numerical method

From the Eq. (1) and Eq. (2), we obtain the advection diffusion equations as follows:

$$\frac{\partial n_s}{\partial t} \pm (\mu_s \boldsymbol{E} \cdot \nabla) n_s$$
$$= \mp n_s (\nabla \cdot \mu_s \boldsymbol{E}) + D_s \nabla^2 n_s + G_s - L_s. \tag{7}$$

To calculate the advection terms in Eq. (7), we employed the M-type CIP (Constrained Interpolation Profile) method [13]. For the time integrations of the non-advection terms in Eq. (7), we also used the 2nd order Runge-Kutta method. We employed the Red-Black SOR (Successive Over Relaxation) method for the calculation of Eq. (5). In order to reduce the calculation load of Eq. (5), the potential distribution of ϕ^{n-1}, which is the results at previous time of $t = n-1$, was used as an initial value for the calculation of ϕ^n. To interpolate the Siglo data base, and data tables obtained by the BOLSIG+, we used the cubic spline method.
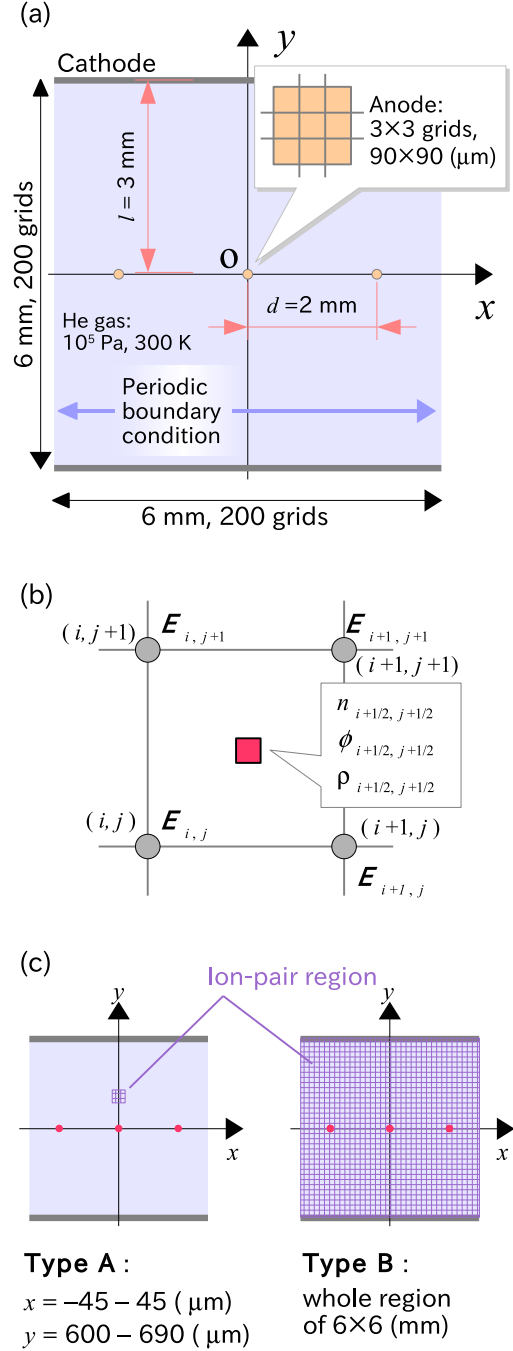

Fig. 1 (a) Schematic diagram of the MWPC configuration. (b) The staggered grid (Arakawa-B grid). (c) The initial distribution of ion-pairs.
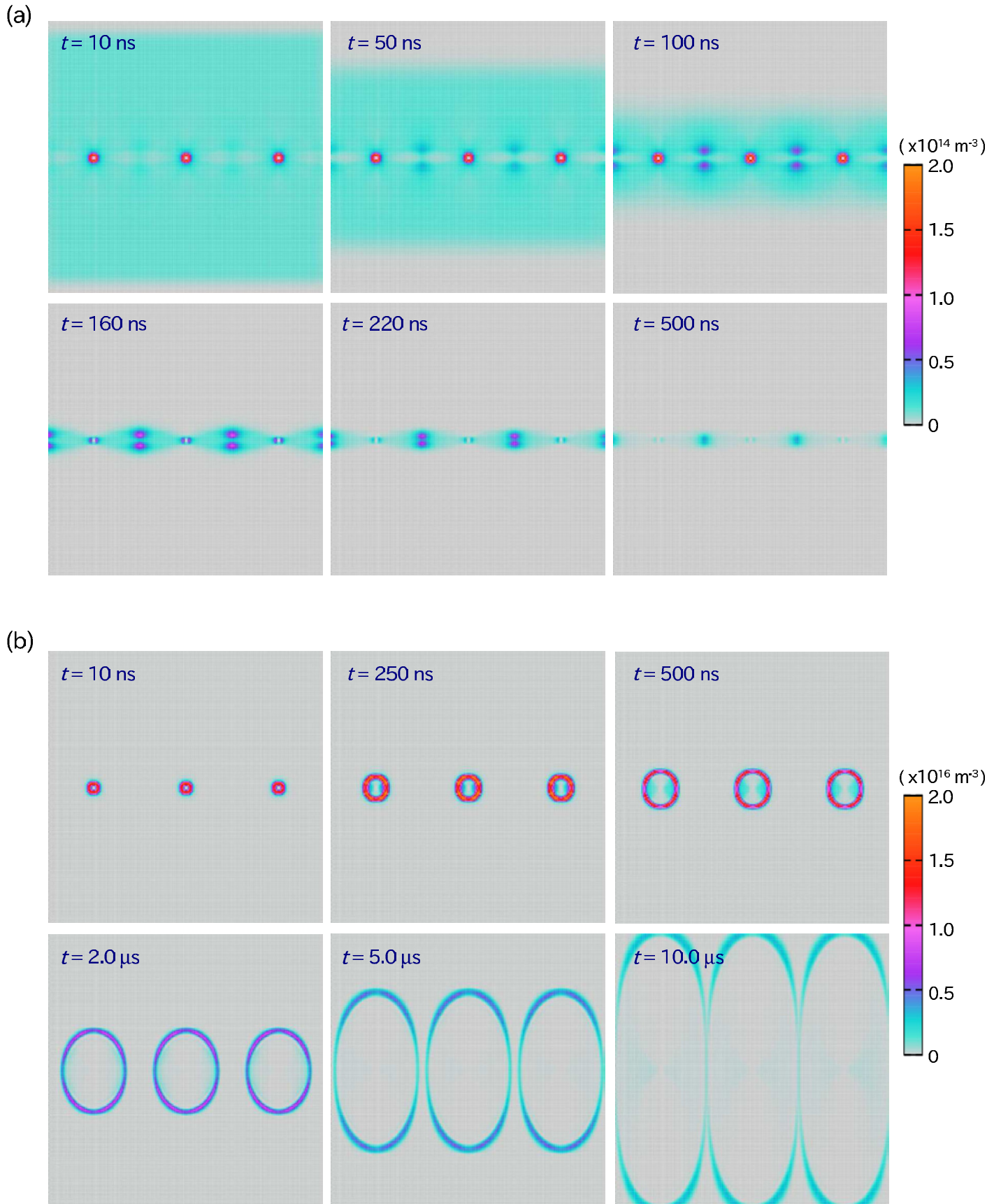
Fig. 2 Temporal evolutions of (a) the electron density distributions, and (b) the ion density distributions.

Fig. 1(a) shows a schematic diagram of the MWPC in a discrete space. For the representation of the multi-wire geometry, we used a rectangular grid. The region of 6×6 mm square was discretized by the staggered grid (Arakawa-B grid, Fig. 1(b)). The anode wires were also represented to be 3×3 rectangular grids (90×90 μm). The outlet boundary condition was applied to the surface of the two cathodes at $y=-3$ and 3, and to the surface of the three anodes. The periodic boundary condition was also applied to the boundaries at $x=-3$ and 3. In this calculation, the initial ion-pairs were distributed as shown in Fig. 1(c). The current signals of the anodes were estimated by calculating the electron flux $I(t)$.

3. Simulation results

A. Temporal evolution of electron/ion distributions

In order to calculate the temporal and spacial evolution of the ion/electron distribution, the initial ion-pairs were homogeneously distributed as the type B in Fig. 1(c) with the density of $N_{\mathrm{init}} = 10^{13}\,\mathrm{m}^{-3}$. The applied voltage of three anodes was $V=1.0\,\mathrm{kV}$.

The temporal evolution of the electron distributions for $t = 10 - 500\,\mathrm{ns}$ are shown in Fig. 2(a). In this case, the electric field distortion by the space charge was enough small to be ignored. The electron avalanches can be seen as increases of the electron density around the anodes. The electron density around anodes is 20 times higher than the initial ion-pair density. Although almost all electrons were gathered into the anodes until $t \simeq 200\,\mathrm{ns}$, a few electrons remained in the regions between the anodes due to the potential valleys where the electric field is small. These remained electrons are finally gathered into the anodes for $\sim 1\,\mu\mathrm{s}$.

The temporal evolution of the ion distributions for $t = 10^{-2} - 10\,\mu\mathrm{s}$ are also shown in Fig. 2(b). In the drift-diffusion approximation procedure, which is applied to evaluate Eq. (1), the advection term of the equation of motion is ignored by assuming the criterion as follows:

$$|\boldsymbol{u}_{\mathrm{s}}| \ll |\boldsymbol{v}_{\mathrm{s,th}}|, \tag{8}$$

where, the $\boldsymbol{v}_{\mathrm{s,th}}$ is the thermal velocity. Around the anodes, the electric field is so high ($E/N_0 \simeq 100\,\mathrm{Td}$, N_0: the density of the neutral particle) that the criterion Eq. (8) for ions cannot be satisfied ($|\boldsymbol{u}_{\mathrm{s}}| \sim |\boldsymbol{v}_{\mathrm{s,th}}| \simeq 10^3\,\mathrm{m/s}$). Therefore the estimation of the ion distribution may be rough around the anodes.

Due to the drift velocity difference between x- and y-directions, the distributions of ions expand elliptically. As the ions move to the cathodes, the density of ions decreased because of the diffusions.

B. Comparisons of the gas gain

For the evaluation of the gas gain, the ion-pairs were distributed as the Type A in Fig. 1(c). In this calculation, the gas gain was calculated from the ratio of the time integrated flux ($= \int I(t)dt$) to initial numbers of ion-pairs. In order to verify the calculation accuracy, numerical results were compared with a theoretical curve. The theoretical gas gain M of the gas chamber, which do not consider the space charge effect, is represented as follows [14]:

$$M = \exp\left\{ \int_{r_{\mathrm{a}}}^{r_{\mathrm{c}}} \alpha(E(r))dr \right\}, \tag{9}$$

where, r_{a} is the radius of the anode, and r is the distance from the center of the anode ($= \sqrt{x^2 + y^2}$). r_{c} is the critical radius of gas multiplication. The critical radius r_{c} is about several times larger than the anode radius r_{a}. In the region far from $r > r_{\mathrm{c}}$, the electric field is too weak to produce the electron avalanches. Therefore, if $r > r_{\mathrm{c}}$, the relation $M(r) \simeq M(r_{\mathrm{c}})$ is satisfied [14]. The intensity of the electric field $E(r)$ of MWPC was derived as a function of x and y [15]:

$$|\boldsymbol{E}(x,y)| =$$
$$\frac{CV}{2\pi\varepsilon_0} \left\{ 1 + \tan^2\left(\frac{\pi x}{d}\right)\tanh^2\left(\frac{\pi y}{d}\right) \right\}^{\frac{1}{2}}$$
$$\times \left\{ \tan^2\left(\frac{\pi x}{d}\right)\tanh^2\left(\frac{\pi y}{d}\right) \right\}^{-\frac{1}{2}}, \tag{10}$$

$$C = \frac{2\pi\varepsilon_0}{\pi l/d - \ln(2\pi r_{\mathrm{a}}/d)}. \tag{11}$$

Here, C is the capacitance per length between the anode and the cathode, V the applied voltage, l the distance between the anode and the cathode, and d the distance between the two anodes.

Fig. 3 shows the comparisons of the numerical results to the theoretical curve. In this numerical calculation, the space charge effect was not considered to be consistent with the theoretical curve. For the evaluation of the theoretical curve, the Townsend first ionization coefficient α was also derived from the Siglo data base. The integration in Eq. (9) was done along the y-axis ($r_{\mathrm{a}} \leq r \leq l$, $l=3\,\mathrm{mm}$). Although there are slight differences, the numerical results agree well with the theoretical curve. We confirmed that our code is capable of quantitative estimation of the gas gain. The slight differences between the numerical results and the theoretical curve are due to the error of the electric field around the anodes, which is caused by the discrete grids. The linearity can be seen for $V > 800\,\mathrm{V}$ in the numerical results.

C. Space charge effect

In order to simulate the gain reduction caused by the space charge effect, the density of initial ion-pairs
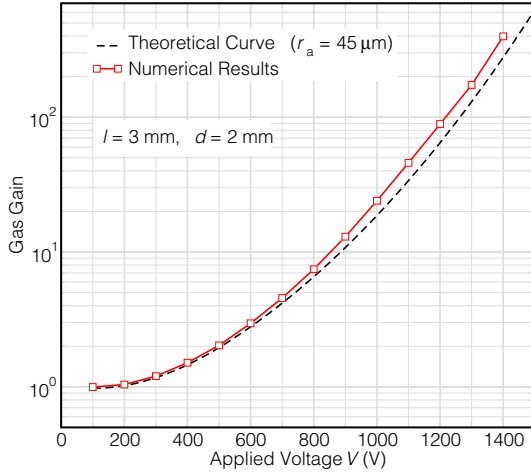
Fig. 3 Comparison of the gas gain obtained from numerical calculation with the theoretical curve.

Fig. 5 Spacial profiles of the ion density distributions.

was increased by $N_{\text{init}} = 10^{15} \, \text{m}^{-3}$. The ion-pair distribution is the type B shown in Fig. 1(c). The applied voltage of the three anodes was $V = 1.0 \, \text{kV}$.

The spacial profiles of the electric field are shown in Fig. 4. The electric field around the anodes decreased drastically for $t = 0 - 100 \, \text{ns}$ as the ion density was increased by the avalanche. On the other hand, the electric field in the region away from the anodes increased. Fig. 5 shows the ion density distributions for $t = 0.1, 0.2, 0.4,$ and $1.0 \, \mu\text{s}$. From these figures, one can see that the region of the distorted electric field moves together with the ions.
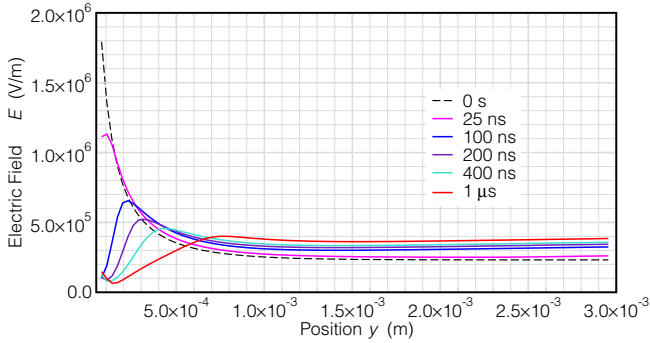

Fig. 4 Spacial profiles of the electric field for $t = 0, 25, 100, 200, 400,$ and $1000 \, \text{ns}$.

Fig. 6 The electric potential distribution at (a) $t=0$ and (b) $t=1 \, \mu\text{s}$.

The electric potential at $t = 0$, which is not distorted by the space charge effect, is shown in Fig. 6(a), the distorted electric potential at $t \simeq 1.0 \, \mu\text{s}$ is also shown in Fig. 6(b). From the comparison between these figures, we found that the electric potential in the region between two anodes is also increased as well as the region around anodes. This is due to the remaining ions in the potential valley between the two anodes.
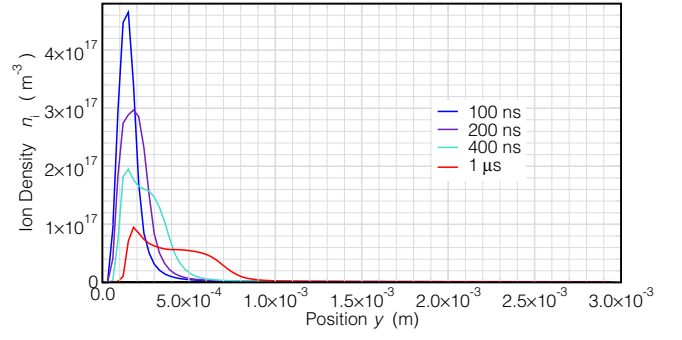
Fig. 7 shows the temporal evolution of the out-

put signal $I(t)$. As a reference, a signal curve without the space charge effect, which can be obtained by neglecting the temporal variation of the electric field from $t = 0$, is also plotted. In this case of the w/o space charge effect, there is a second hump in the signal curve. This is due to the electrons which move through the region of the weak electric field (around the potential valley), and arrive at the anodes later than those gathered directly. The reduction of the
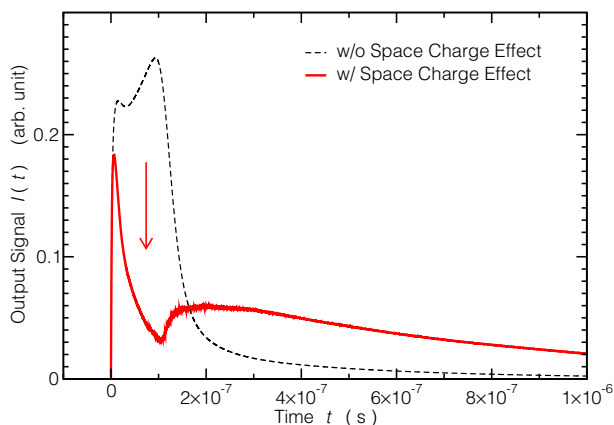
Fig. 7 Signal current reduction due to the space charge effect.

signal cased by the space charge effect can be clearly seen. Because the ion-pairs are initially distributed as the type B shown in Fig. 1(c), the transient signal as shown Fig. 7 was seen. The signal intensity begin to increase again at $t = 100$ ns. This increase of the signal may be explained by the arrival delay of the electrons, which are multiplied before the decrease of the electric field, and drift slowly by the decreased electric field around the anodes.

4. Conclusion

In order to optimize the MWPC for the high rate incident projectiles, we developed a numerical code by employing a two-dimensional continuum model. We confirmed that the calculation code has capability to estimate the gas gain quantitatively. For the increased uniform distribution of the ion-pairs, the space charge effect was seen as the distortion of the electric field and the electric potential. Also, the gain reduction caused by the space charge effect was clearly seen as a decrease of the transient signal current. If the incident projectiles continue to enter the MWPC and to make the ion-pairs after the formation of the distorted field as shown in Fig. 6(b), the decrease of the signal is expected to be seen successively. In order to examine further the capability of the quantitative estimation on the gas gain, this output signal needs to be compared with the results obtained by the beam experiments at HIMAC.

5. Acknowledgements

[1] T. Furukawa, N. Saotome, et al., Med. Phys., **35**, 2235 (2008).

[2] M. Torikoshi, K. Noda, et al., Nucl. Instrum. Meth. A, **435**, 326 (1999).
[3] E. Mathieson, Nucl. Instrum. Meth. A, **249**, 413 (1986).
[4] E. Mathieson, G.C. Smith, Nucl. Instrum. and Meth. A, **316**, 246 (1992).
[5] W. Riegler, C. Lippmann, et al., Nucl. Instrum. and Meth. A, **582**, 469 (2007).
[6] T. Sakae, A. Nohtomi, Nucl. Instrum. and Meth. A, **397**, 323 (1997).
[7] S. Kato, et al., J. Plasma Fusion Res., **84**, 477 (2008).
[8] F. Tochikubo, H. Arai, Jpn. J. Appl. Phys., **41**, 844 (2002).
[9] P. Hartmann, H. Matsuo, et al., Jpn. J. Appl. Phys., **42**, 3633 (2003).
[10] T. Fujimoto, et al., Journal of the Spectroscopical Society of Japan, **34**, 347 (1985)
[11] G.J.M. Hagelaar and L.C. Pitchford, Plasma Sources Sci. Technol. **14**, 722 (2005)
[12] The Siglo data base, CPAT and Kinema Software, ⟨http://www.siglokinema.com⟩.
[13] T. Yabe, T. Aoki, Comput. Phys. Comm., **66**, 219 (1991).
[14] Glenn F. Knoll, *Radiation Detection and Measurement* (Wiley, New York, 2000).
[15] F. Sauli, *Principles of Operation of Multiwire Proportional and Drift Chamber*, CERN Report 77-09 (1977).